Bergische Universität Wuppertal

Fakultät für Mathematik und Naturwissenschaften

Institute of Mathematical Modelling, Analysis and Computational Mathematics (IMACM)

Preprint BUW-IMACM 22/08

Matthias Ehrhardt, Sergey Pereselkov, Venedikt Kuz'kin, Ilya Kaznacheev and Pavel Rybyanets

Experimental Observation and Theoretical Analysis of the Low-frequency Source Interferogram and Hologram in Shallow Water

March 16, 2022

http://www.imacm.uni-wuppertal.de

Article

Experimental Observation and Theoretical Analysis of the Low-frequency Source Interferogram and Hologram in Shallow Water

Matthias Ehrhardt [1,*], Sergey Pereselkov [2], Venedikt Kuz'kin [3], Ilya Kaznacheev [2] and Pavel Rybyanets [2]

[1] University of Wuppertal, Gaußstraße 20, 42119 Wuppertal, Germany; ehrhardt@uni-wuppertal.de
[2] Voronezh State University, Russia; pereselkov@yandex.ru
[3] Prokhorov General Physics Institute of the Russian Academy of Sciences, Russia; kumiov@yandex.ru
* ehrhardt@uni-wuppertal.de; pereselkov@yandex.ru;

Abstract: The interference pattern of the sound field of a broadband source in a shallow water waveguide is studied theoretically and experimentally in this paper. In the ocean waveguide, the sound source generates the interference pattern of the intensity distribution (interferogram) in the frequency-time domain. The mathematical theory of the interferogram structure is developed. The source interferogram consists of a set of quasi-parallel interference fringes in the frequency-time domain. It is shown that the slope of the interference fringes depends on the distance, velocity, and direction of motion of the sound source. The relationship between the slope angle of the interference fringes in the interferogram and the source parameters is derived in the paper. The two-dimensional Fourier transform (2D-FT) is used to analyze the interferogram. The result of the 2D-FT is called the Fourier hologram (hologram). It is shown that the hologram consists of a few focal spots in a relatively small area. The presence of these focal spots is the result of the interference of acoustic modes with different wavenumbers. The mathematical theory of the hologram structure is developed in this paper. The relationship between the coordinates of the focal spots on the hologram and the source parameters is considered. Consequently, the position of the focal spots can be used to estimate the source parameters (range, velocity, and direction of motion). The theoretical conclusions are verified in the context of computer modeling and the results of the acoustic experiment on the Pacific shelf (Yellow Sea, 2004) in the band 180–220 Hz.

Keywords: sound field; waveguide; interference pattern; hologram; source detection; vector sensor; signal processing

PACS: 43.30.+m; 43.60.-c; 43.60.Vx; 02.30.Nw

Citation: Ehrhardt, M.; Pereselkov, S.; Kuz'kin, V.; Kaznacheev, I.; Rybyanets, P. Title. *Sensors* **2022**, *1*, 0. https://doi.org/

Received:
Accepted:
Published:

Publisher's Note: MDPI stays neutral with regard to jurisdictional claims in published maps and institutional affiliations.

1. Introduction

The interference pattern of the sound field of a broadband source in a shallow water waveguide was studied experimentally and theoretically. The acoustic experiment was conducted on the Pacific shelf (Yellow Sea, 2004). The acoustic signals were emitted from the airgun source (with a frequency band of 10–250 Hz). The source was towed at a speed of 1.7 m/s at a depth of 15 m along different paths. The bottom receivers at a depth 53 m was used to record the acoustic signals. The experimental recordings were processed to obtain sound intensity distributions (interferograms) $I(\omega, t)$ in the frequency-time domain for different paths of the source motion. The two-dimensional Fourier transform (2D-FT) is applied to analyze the experimental interferograms $F(\tau, \nu)$.

The interference of the normal modes of the sound field in underwater waveguides leads to certain patterns to be observed in the sound intensity distribution in the frequency domain (Chuprov [2]) or the the frequency-time domain (Weston and Stevens [1]). In this context, let us note that the mathematical theory of sound field interference in underwater acoustics was developed by the pioneering work of Chuprov [2] hereby introducing the waveguide invariant - an essential parameter of the interference pattern in the sound field.

The normal mode interference of the sound field in underwater waveguides leads to structured patterns that can be observed in the sound intensity distribution in the frequency-time domain (Weston and Stevens [1]) or in the frequency-range domain (Chuprov [2]). The theory of sound field interference in underwater acoustics was developed by Chuprov [2]. He introduced the concept of the waveguide invariant – a fundamental parameter of the interference pattern in the sound field. The more significant achievements in interference theory are presented in the following papers: Grachev [3], Orlov and Sharonov [4] and papers of Conf. Proc. edited by Kuperman and D'Spain [5]. The developed interference theory in ocean waveguides allowed solving a number of important problems in underwater acoustics: source localization (passive mode [6–16] and active mode [17,18]), remote sensing of geo-acoustic parameters [19], effective signal processing [20–22].

One of the most important advances in interference theory is the interference pattern analysis approach [23–26]. In this approach, the interference pattern is considered as the sound intensity distribution $I(\omega, r)$ in the frequency domain or $I(\omega, t)$ in the frequency-time domain and the 2D Fourier transform (2D-FT) of $I(\omega, r)$ is used to analyse sound intensity distributions. With this approach, the waveguide invariant [24,27] can be estimated first. The estimate of the waveguide invariant is the extremum of the "reference" distribution of the 2D-FT. Secondly, this approach allows the coherent accumulation of the sound intensity of the interferogram in a narrow region as focal spots and significantly increases the signal-to-noise ratio (SNR) [6,9].

Matched field processing (MFP) [28–30] for passive localisation estimates of the range and depth of the source are taken into account. The application of MFP needs a priori information about the model waveguide (such as water layer and the soil). MFP is based on a spatial filter for acoustic signals received by an antenna; it includes methods like Bartlett's method [31,32], Capon's method [33,34] and MUSIC's method [35,36]. The main limitations of the MFP methods are inaccuracies in the acoustic parameters of the model waveguide, source motion and low robustness to noise. In addition, the MFP method does not allow the range of the source and its velocity to be estimated in a single computational process without numerous iterations of the values. Overcoming these difficulties is associated with the development of an interferometric method for localising the moving source.

The mathematical theory of the interferogram structure is developed in this paper. The source interferogram consists of a set of quasi-parallel interference fringes in the frequency-time domain. It is shown that the slope of the interference fringes depends on the distance, velocity, and direction of motion of the sound source. The relationship between the slope angle of the interference fringes in the interferogram and the source parameters is derived in the paper. We recall that the result of the 2D-FT is called a Fourier hologram (hologram). It is shown that the hologram consists of a few focal spots in a relatively small area. The presence of these focal spots is the result of the interference of acoustic modes with different wavenumbers. The mathematical theory of the hologram structure is developed in this paper. The relationship between the coordinates of the focal spots on the hologram and the source parameters is considered. Consequently, the position of the focal spots can be used to estimate the source parameters (range, velocity, and direction of motion). The theoretical conclusions are verified in the context of computer modeling and the results of the acoustic experiment on the Pacific shelf.

This paper consists of seven sections. The experiment on the Pacific shelf is described in Section 2. The mathematical theory of the interferogram of the moving broadband sound source is developed in Section 4. The theory of the hologram of the moving broadband sound source is discussed in Section 5. The results of numerical simulation of the interferogram and the hologram for the acoustic experiment conditions are presented for different paths of the source motion in Section 6. The experimental results of the interferograms and holograms are considered in Section 7 for different paths of the source motion. It is shown that the position of the focal points in the experimental hologram depends on the radial velocity of the source, the direction of motion and the distance to the receiver.

Consequently, the displacement of the focal points in the hologram domain can be used to estimate the above source parameters.

2. The Experiment

Let us briefly describe the setting of our experiment that was conducted in 2004 on the Pacific shelf (Yellow Sea). First, the environmental parameters: water depth $H \approx 53$ m, sound velocity in the water layer $c \approx 1474$ m/s. Next, we turn to the acoustic parameters. The airgun was used as a broadband sound source and the sound source with depth $z_s \approx 15$ m was towed by a research vessel with speed $v \approx 1.7$ m/s. The airgun had a pulse signature that proved to be quite repeatable. The signal pulses were controlled by a monitor hydrophone located at a distance of 2 m from the source. The airgun produced broadband pulses, separated by a time interval $T = 30$ s, that consistently exhibited repeatable spectra in the range of $\delta f \approx 10 - 250$ Hz.

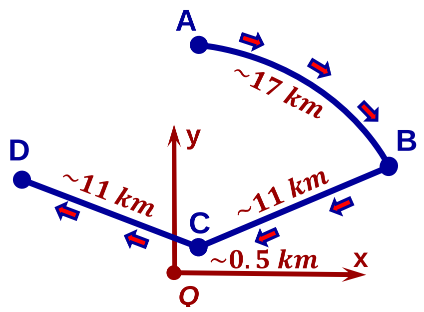

Figure 1. The experimental scheme. View from above.

In Fig. 1 we illustrate the movement if the towed airgun source, including the stationary position of the vector scalar receiver (VSR) Q. It can be clearly seen, atht the source moved along an arc of radius $r_0 \approx 11$ km from the starting point A to point B. At point B, the source motion became a straight line and in the sequel the approached VSR Q on a straight line path from point B to point C close to the receiver VSR Q. At point C the source was rotated and moved along a straight line away from VSR Q to point D.

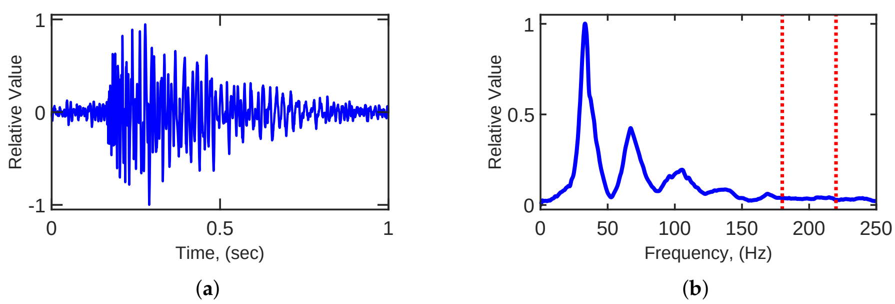

Figure 2. The experimental airgun pulse: (a) time dependence; (b) normalized spectrum.

During the experiment, signals from the airgun source were received by the VSR, which had channels for measuring the pressure and the three components of the vibration velocity. The pressure measurement results from the VSR, located at a depth of $z_q \approx 53$ m, are used for the signal processing presented in this paper. The example of the received signal is shown in Fig. 2. The normalized time dependence of the received signal is shown in Fig. 2(b). The normalized spectrum of the received signal is shown in Fig. 2(b). The received signals are analyzed in the band $\Delta f \approx 180 - 220$ Hz. The amplitude of the airgun pulses was normalized to the same value to keep the contrast of the interference patterns constant.

The experimental waveguide bottom parameters are determined by the maximal match between the experimental received signal and the numerical simulation results. The time dependence of the normalized signal envelope in the band 180-220 Hz: are shown in Fig. 3: (a) experiment; (b) simulation. The vertical dotted lines show the $m-th$ mode propagation times; $m = 1-5$. The waveguide bottom parameters for maximal match: refractive index is $0.86(1+i0.01)$, density $\rho_b = 1.8\ \mathrm{g/cm^3}$ (see Fig. 3). The mode parameters for maximal match are given in Table 1

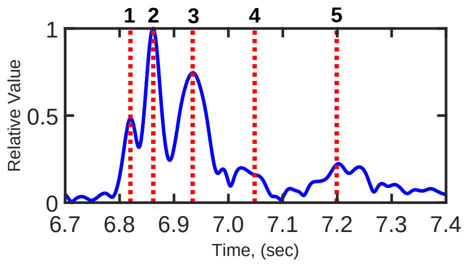

(**a**)

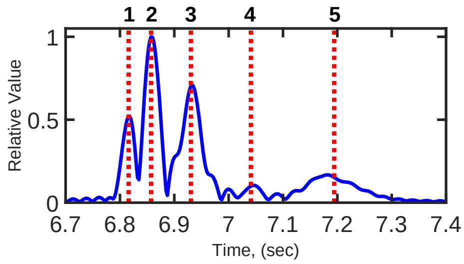

(**b**)

Figure 3. Time dependence of the normalized signal envelope in band 180–220 Hz: (a) experiment; (b) simulation. The vertical dotted lines show the m-th mode propagation times; m=1-5.

Table 1. Mode parameters

Mode	Wave Number ($\mathrm{m^{-1}}$)	Group Velocity (m/s)
1	0.8488	1467.0
2	0.8420	1455.3
3	0.8284	1438.4

3. The Sound Field in Shallow Water Waveguide

In this section we introduce the mathematical tools behind our research work. We use a Cartesian coordinate system $(\vec{r}, z)$ and consider an oceanic waveguide as a water layer between the ocean surface ($z = 0$) and the shallow bottom surface ($z = H$). Fig. 4 shows a schematic of this water waveguide geometry. In our model the refractive index and density of the water layer are denoted by $n(z)$, $\rho(z)$. Next, the complex refractive index and the density of the soil are denoted by $n_b(1+i\alpha)$, ρ_b. Further, the parameter α is determined by the absorption properties of the soil.

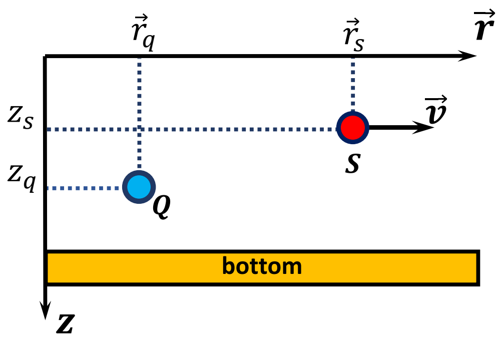

Figure 4. The waveguide model. Vertical plane.

The receiver is located at the point $Q(\vec{r}_q, z_q)$. The broadband sound source is moving at the point $S(\vec{r}_s(t), z_s(t))$. The source velocity is denoted by $\vec{v}$. The spectrum of the signal radiated by sound source is $S(\omega)$. Here, $\omega = 2\pi f$ is the sound frequency. The sound field in the shallow water waveguide is the solution of the following boundary problem

$$\begin{cases} \Delta p + k^2(\vec{R})p = -S(\omega)\,\delta(\vec{r}-\vec{r}_s)\,\delta(z-z_s), & 0 < z < H, \\ \Delta p_b + k_b^2 p_b = 0 & z \geqslant H, \end{cases} \tag{1}$$

supplied with boundary conditions

$$\begin{gathered} p(\vec{R})|_{z=0} = 0, \quad p(\vec{R})|_{z=H} = p_b(\vec{R})|_{z=H}, \\ \frac{\partial p(\vec{R})}{\partial z}\Big|_{z=H} = \eta \frac{\partial p_b(\vec{R})}{\partial z}\Big|_{z=H}. \end{gathered} \tag{2}$$

The complex sound pressure can be written as follows, cf. [30,37]:

$$p(r,\omega,z_s,z_q) = S(\omega)\,\frac{\mathrm{i}\,e^{-\mathrm{i}\pi/4}}{\rho(z_s)\sqrt{8\pi}} \sum_m^M \frac{\phi_m(z_s,\omega)\,\phi_m(z_q,\omega)\,\exp\big[\mathrm{i}rh_m(\omega)\big]}{\sqrt{rh_m(\omega)}}, \tag{3}$$

where $r = |\vec{r}_q - \vec{r}_s|$ denotes the distance between source and receiver. $h_m(\omega)$ denotes the horizontal wavenumber of the m-th acoustic mode, where $\phi_m(z,\omega)$ is the respective acoustic mode. In (3) the summation is performed up to M, the total number of acoustic modes to be considered. Finally, we recall the standard assumption that the source depth z_s and the receiver depth z_q are constant. Consequently, the sound pressure depends on the sound frequency ω and the distance r between source and receiver.

Using the acoustic vertical modes, one obtains for the pressure field Eq. (1). The $\phi_m(z,\omega)$ are the eigenfunctions (modes) and $h_m(\omega)$ and $\gamma_m(\omega)/2$ are the real and imaginary parts of the eigenvalues (horizontal wave numbers) $\xi_m(\omega) = h_m(\omega) + \mathrm{i}\gamma_m(\omega)/2$ obtained by solving the Sturm-Liouville problem subject to the usual boundary conditions [30]

$$\begin{gathered} \frac{d^2\phi_m(z)}{dz^2} + k^2\phi_m(z) = \xi_m^2\phi_m(z), \\ \phi_m(z)\big|_{z=0} = 0, \\ \phi_m(z)\big|_{z=H} + g(\xi_m)\frac{d\phi_m(z)}{dz}\Big|_{z=H} = 0. \end{gathered} \tag{4}$$

4. The Interferogram of the Moving Source

In this section we investigate the interference pattern of the intensity distribution (interferogram) in the frequency-time domain. In the framework of the normal mode analysis to describe the sound pressure field Eq. (1), the interferogram $I(\omega,r)$ reads

$$I(\omega,r) = |p(\omega,r)|^2 = \sum_m^M \sum_n^M A_m(\omega,r)A_n^*(\omega,r)\,\exp\big[\mathrm{i}rh_{mn}(\omega)\big], \tag{5}$$

where

$$\begin{gathered} A_m(\omega,r) = S(\omega)\frac{\mathrm{i}e^{-\mathrm{i}\pi/4}}{\rho(z_s)\sqrt{8\pi}}\frac{\phi_m(z_s,\omega)\,\phi_m(z_q,\omega)}{\sqrt{rh_m(\omega)}}, \\ h_{mn}(\omega) = h_m(\omega) - h_n(\omega). \end{gathered} \tag{6}$$

In equations (5), (6) $A_m(\omega,r)$ denotes the amplitude of the m-th mode and the superscript $*$ indicates complex conjugation. Here, the modes exhibit an amplitude dependence, accounting for the cylindrical divergence of the field, the modal damping coefficients, and the depths of the source z_s and the receiver z_q. In the sequel, we will drop the sound intensity arguments, because the depths of the source and receiver do not affect the structure of the interferogram in the range (ω,r).

The interferogram $I(\omega, r)$ can be represented as the sum of partial interferograms $I_{mn}(\omega, r)$ produced by interference of m-th and n-th modes.

$$I(\omega, r) = \sum_{m}^{M}\sum_{n}^{M} I_{mn}(\omega, r), \tag{7}$$

where

$$I_{mn}(\omega, r) = A_m(\omega, r)A_n^*(\omega, r)\ \exp\left[irh_{mn}(\omega)\right]. \tag{8}$$

Let us consider the interferogram $I(\omega, r)$ in the frequency band $\omega_0 - \Delta\omega/2 \leq \omega \leq \omega_0 + \Delta\omega/2$. The signal spectrum $S(\omega)$ is assumed to be constant for this frequency band. Therefore, the variation of the interferogram with frequency is due to the dependence of the horizontal wavenumbers on frequency. In the case of a moving source, the distance between the source and receiver is a function of time:

$$r(t) = \left|\vec{r}_q - \vec{r}_s(t)\right|. \tag{9}$$

So, the interferogram $I(\omega, r(t)) = I(\omega, t)$ can be considered frequency-time domain $\omega_0 - \Delta\omega/2 \leq \omega \leq \omega_0 + \Delta\omega/2$, $0 \leq t \leq \Delta t$. The source-receiver distance increment within the observation time Δt is:

$$\Delta r(t) = r(t) - r_0. \tag{10}$$

Here, the initial source-receiver distance is $r(t_0) = r_0$ at the initial time t_0. When the horizontal distance between the source and the receiver changes, the frequency shift $\Delta\omega$ can be described as follows

$$\Delta\omega(t) = \beta\omega_0\frac{\Delta r(t)}{r_0}, \tag{11}$$

where (ω_0, r_0) are the initial coordinates of the observed local field maximum; $\Delta\omega(t) = \omega(t) - \omega_0$ and $\Delta r = r(t) - r_0$ are, the frequency and distance increments, respectively, corresponding to the shift of the observed maximum in the $\omega - r$ plane; and β is an interference invariant characterizing the slope of a localized fringe [2]. The β value can be determined by one of the methods developed to date [23].

Considering that the distance traveled by a source is $\rho(t) = vt$ and that the difference in distances between the observation point and the source positions (accurate to the smallness terms ρ^2/r_0^2)

$$\Delta r(t) = r(t) - r_0 = \rho(t)\left[\cos\varphi + \frac{\rho(t)\sin^2\varphi}{2r_0}\right]. \tag{12}$$

where φ is the angle between the source-receiver direction and the source motion direction. The expression can be written as

$$\omega(t) = \omega_0 + \beta\omega_0\frac{\rho(t)\left(\cos\varphi + \rho(t)\sin^2\varphi/2r_0\right)}{r_0} = \omega_0 + \Delta\omega(t). \tag{13}$$

The frequency shift is thus determined by both the linear projection $v_r = v\cos\varphi$ (the radial component) and the quadratic projection $v_\tau^2 = (v\sin\varphi)^2$ (the tangential component) of the source velocity. Thus, when the object is moving, the interference pattern in the frequency-time plane (ω, t) is generally formed by curved localized fringes determined by the quadratic dependence

$$\Delta f(t) = b^2\left(t + \frac{a}{2b^2}\right)^2 - \left(\frac{a}{2b}\right)^2, \tag{14}$$

where $a = \beta\omega_0 v_r/r_0$ and $b^2 = \beta\omega_0 v_\tau^2/2r_0^2$. It can be seen that increasing the initial distance r_0 and a decreasing the velocity v and angle φ decrease the degree of fringe curvature. In particular, when $\varphi = 0$, $\Delta\omega(t) = at$; i.e., the fringes are described by $\Delta\omega(t) = b^2t^2$ [16], and the fringes are maximally curved. Note that the above analysis suggests the smallness of ρ^2/r_0^2, which limits the signal accumulation time t, depending on the source velocity v and the initial source-receiver distance r_0: $t^2 \ll r_0^2/v^2$. According to (14) the slope of the interference fringe is

$$\varepsilon_\omega(t) = \frac{d\Delta\omega(t)}{dt} = 2b^2\Big(t + \frac{v_r r_0}{v_\tau^2}\Big). \tag{15}$$

Hence, the fringe curvature can be neglected (assuming that $\varepsilon(t) \approx$ const) if

$$\frac{\rho}{r_0} \ll \frac{\cos\varphi}{\sin^2\varphi}. \tag{16}$$

This is the condition under which the tangential component of the velocity is small compared to the radial component. In this case, the second term in brackets in (14) can be neglected.

If the inequality (16) is valid, one can determine the object velocity using the approach proposed in [23], which is applied to determine the interference invariant β (11). The expression for the latter has the following form in the considered case:

$$\beta = \frac{r_0}{\omega_0}\frac{\varepsilon_\omega}{v_r}. \tag{17}$$

Let us analyze the interference component $u(\omega, t) = I(\omega, t) - \overline{I(\omega, t)}$, where $\overline{I(\omega, t)}$ is the $I(\omega, t)$ field smoothed over spatial and frequency interference beatings in the frequency-time domain $-\Delta\omega/2 + \omega_0 \le \omega \le \omega_0 + \Delta\omega/2$, $0 \le t \le \Delta t$. Beyond this window, $u(\omega, t) = 0$. Let us pass to sound frequency $f = \omega/2\pi$:

$$\beta = \frac{r_0}{f_0}\frac{\varepsilon}{v_r}. \tag{18}$$

Taking into account the linear time dependence of the frequency shifts, we then obtain the position of the maximum of the functional (see Fig. 5).

$$\Phi(\varepsilon_*) = \int_{f(t)-\Delta f}^{f(t)+\Delta f} u(t, f)\, df, \tag{19}$$

which corresponds to the radial velocity component $v_r = v\cos\varphi$. Here, Δf is the interference-fringe width and

$$f(t) = f_0 + \varepsilon t. \tag{20}$$

Physically, this process means the accumulation of spectral intensity along the interference fringes formed by a moving source (see Fig. 5). The maximum of (19) is reached when the fringe slope is determined by the source velocity projection v_r. Note that with this approach the radial velocity component v_r can be determined at an unknown angle φ. If the condition (16) is not fulfilled, the use of the algorithm (19) leads to an error in the determination of v_r, which increases with the time of the trace analysis. Among the numerous variants, the approximation of a very fast noise source is the most dangerous. In this case, a fast estimate of the approximation velocity in passive mode is particularly urgent.

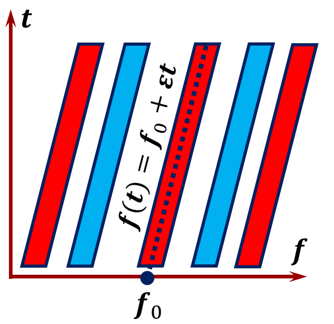

Figure 5. The structure of the interferogram of a moving source and angular interferogram distribution $\Phi(\varepsilon)$.

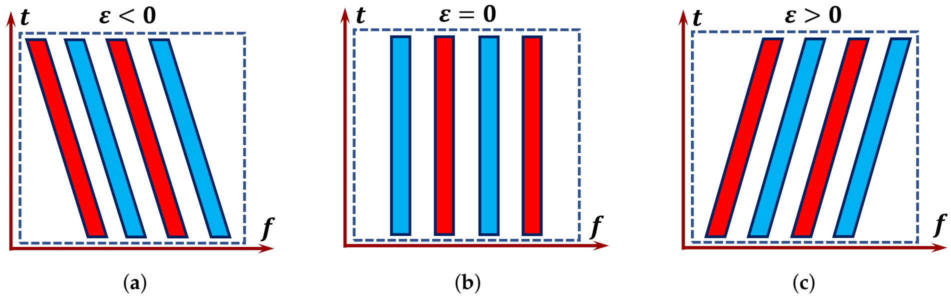

Figure 6. The structure of the interferogram for different cases of the source moving: (a) source moves to receiver; (b) distance between source and receiver is constant; (c) source moves from receiver.

162 The structure of the interferogram is shown in Fig. 6 for different cases of the source moving. The Fig. 6 (a) is corresponds to source moving to receiver. The slope ratio of the interference fringes is negative. As results maximum of the $\Phi(\varepsilon)$ is for $\varepsilon < 0$. The Fig. 6 (b) is corresponds to constant distance between source and receiver. The slope ratio of the interference fringes is zero for this case. So, maximum of the $\Phi(\varepsilon)$ is for $\varepsilon = 0$. The Fig. 6 (c) is corresponds to source moving from receiver. The slope ratio of the interference fringes is positive. As results maximum of the $\Phi(\varepsilon)$ is for $\varepsilon > 0$.

5. The Hologram of the Moving Source

Consider a hologram of the sound source in an oceanic waveguide. We apply a two-dimensional Fourier transform (2D-FT) to the interferogram $I(\omega, t)$ (Eq. (5)) in the frequency-time variables (ω, t). The result of the 2D-FT is called Fourier hologram (hologram) $F(\tilde{\nu}, \tau)$:

$$F(\tilde{\nu}, \tau) = \sum_m \sum_n F_{mn}(\tilde{\nu}, \tau), \tag{21}$$

where $\tilde{\nu} = 2\pi\nu$ is the cyclical frequency of the hologram domain, τ is time of the hologram domain. Let us analyze the term on the right-hand side of Eq. (21):

$$F_{mn}(\tilde{\nu}, \tau) = \int_0^{\Delta t} \int_{\omega_0 - \frac{\Delta\omega}{2}}^{\omega_0 + \frac{\Delta\omega}{2}} I_{mn}(\omega, t) \exp\left[\mathrm{i}(\tilde{\nu}t - \omega\tau)\right] dt d\omega. \tag{22}$$

We use a linear approximation of the horizontal wavenumber $h_m(\omega)$ as a function of frequency:

$$h_m(\omega) = h_m(\omega_0) + \frac{dh_m(\omega_0)}{d\omega}(\omega - \omega_0). \tag{23}$$

Then we assume that modes with numbers close to the l-th mode interfere constructively. Considering the number of modes as a continuous variable, we obtain

$$F_{mn}(\tilde{v},\tau) = A_m A_n^* \exp\left[\mathrm{i}\left(\frac{\tilde{v}\Delta t}{2} - \tau\omega_0\right)\right]\Delta\omega\Delta t \exp\left\{\mathrm{i}(m-n)\alpha\left(\frac{\Delta t}{2}v_r + r_0\right)\right\}$$
$$\times \frac{\sin\left\{\left[(r_0+v_r t_{mn})(m-n)\frac{d\alpha}{d\omega} - \tau\right]\frac{\Delta\omega}{2}\right\}}{\left[(r_0+v_r t_{mn})(m-n)\frac{d\alpha}{d\omega} - \tau\right]\frac{\Delta\omega}{2}} \frac{\sin\left\{\left[v_r(m-n)\alpha + \tilde{v}\right]\frac{\Delta t}{2}\right\}}{\left[v_r(m-n)\alpha + \tilde{v}\right]\frac{\Delta t}{2}}, \qquad (24)$$

where $\alpha = dh_l(\omega_0)/dl$. The introduction of the expansion in equation (23) turns out to be useful for the interpretation of the hologram structure. In fact, according to Eq. (23)

$$\frac{d\alpha}{d\omega}(m-n) = \frac{dh_{mn}(\omega_0)}{d\omega}, \qquad \alpha(m-n) = h_{mn}(\omega_0).$$

Here $d\omega/dh_m = u_m$, is the group velocity of the m-th mode.

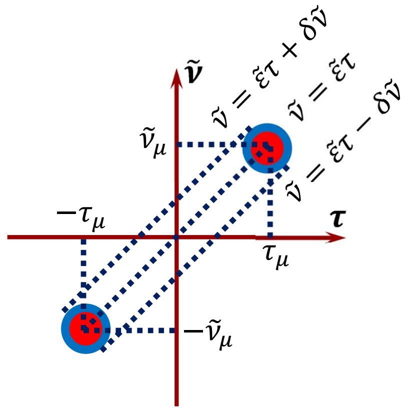

Figure 7. The partial hologram structure - $F_{mn}(\tau,\tilde{v})$. The focal spots are at points with coordinates $(\tau_\mu,\ \tilde{\nu}_\mu)$ and $(-\tau_\mu,\ -\tilde{\nu}_\mu)$.

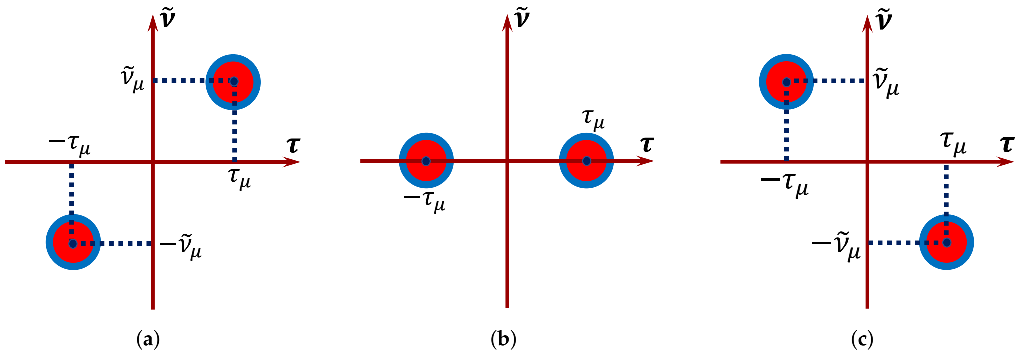

Figure 8. The partial hologram structure - $F_{mn}(\tau,\tilde{v})$ for different cases of the source moving: (a) source moves to receiver; (b) distance between source and receiver is constant; (c) source moves from receiver.

The hologram Eq. (24) is localized in two domains symmetrical to the origin of the plane $(\tilde{v},\tau)$ (Fig. 7). This property of the hologram is the result of the function symmetry (Eq. (24)): $F_{mn}(\tilde{v},\tau) = F_{nm}(-\tilde{v},-\tau)$. The hologram is located in quadrants I and III of the plane $(\tilde{v},\tau)$ when the radial velocity $v_r < 0$, i.e. the angle of the trajectory $\pi/2 < \varphi \leq \pi$ (Fig. 8 (a)). The hologram is located on the τ-axis of the plane $(\tilde{v},\tau)$ when the radial velocity

$v_r = 0$, i.e. the distance between the source and the receiver is constant (Fig. 8 (b)). The hologram is located in quadrants II and IV of the plane $(\tilde{\nu}, \tau)$ when the radial velocity $v_r > 0$, i.e. the angle of the trajectory $0 \leq \varphi < \pi/2$ (Fig. 8 (c)). Thus, based on the hologram, one can estimate whether the source is moving away from the receiver or toward the receiver. The positions of the main maxima of the hologram can be estimated as follows

$$\begin{aligned} \tau_{mn} &= (r_0 + v_r t_{mn})(m-n)\frac{d\alpha}{d\omega}, \\ \tilde{\nu}_{mn} &= -v_r(m-n)\alpha\,. \end{aligned} \tag{25}$$

In other words, the positions of the focal spot maxima in the hologram are proportional to the radial velocity v_r and the initial distance between the source and the receiver (r_0).

The values t_{mn} are limited to a small neighborhood of a point t_1 in the observation interval Δt ($0 < t_1 < \Delta t$), and it is possible to use $t_{mn} \approx t_1$. Doing so, the results remain quite reasonable qualitatively and quantitatively, as seen below.

In this case, the localization region $(M-1)$ contains main maxima with coordinates $(\tau_\mu,\ \tilde{\nu}_\mu)$, as shown in Fig. 7. Here $\mu = 1, \ldots, M-1$ is the number of focal spots that are located on the line $\tilde{\nu} = \tilde{\varepsilon}\tau$. The focal spot peak closest to the origin of the hologram coordinate system is due to the interference of adjacent modes $(m,\ m+1)$. It is located at the point $(\tau_1,\ \tilde{\nu}_1)$. The adjacent focal point caused by the interference of modes numbered $(m,\ m+2)$ is located at the point $(\tau_2, \tilde{\nu}_2)$, etc. The coordinates of the farthest peak are determined by the interference of the first and last modes – $(\tau_{M-1}, \tilde{\nu}_{M-1})$. At points with coordinates $(\tau_\mu,\ \tilde{\nu}_\mu)$ main peaks are summed up.

The main maximum of the spectral density is located in the first focal point. It can be deduced [12] that the slope ratio of the line $\tilde{\nu} = \tilde{\varepsilon}\tau$ is

$$\tilde{\varepsilon} = \langle \tilde{\nu}_\mu / \tau_\mu \rangle, \tag{26}$$

where the angle brackets denote averaging over focal spot numbers. we emphasize that the slope ratio of the line $\tilde{\nu} = \tilde{\varepsilon}\tau$ on the hologram and the slope ratio interference fringes are the same. Therefore,

$$\tilde{\varepsilon} = -\delta\omega/\delta t, \tag{27}$$

where $\delta\omega$ denotes the field maximum frequency shift during the time δt.

On the hologram, the spectral density is mainly concentrated in the band between straight lines (see Fig. 7)

$$\tilde{\nu} = \tilde{\varepsilon}\tau + \delta\tilde{\nu}, \quad \tilde{\nu} = \tilde{\varepsilon}\tau - \delta\tilde{\nu}, \tag{28}$$

where $\delta\tilde{\nu} = 2\pi\Delta t$ is the bandwidth along the frequency axis. Outside this band, the spectral density practically vanishes.

The spectral density distribution in different directions $\tilde{\varepsilon}_*$ is described by the function [24]

$$G(\tilde{\varepsilon}_*) = \int_0^{\Delta\tau} \left|F(\tau, \tilde{v}(\tau))\right| \sqrt{1+\tilde{\varepsilon}_*^2}\, d\tau. \tag{29}$$

Here, $\Delta\tau$ is the linear size of the localization region along the τ-axis. In absence of the noise, the maximum position of the function (Eq. (29)) is equal to the value of $\tilde{\varepsilon}$. $G(\tilde{\varepsilon}_*)$ is called the angular hologram distribution in our paper.

The focal spot maxima coordinates are proportional to the radial velocity and the initial source distance from the receiver.

$$\hat{v}_r = -\kappa_{w\mu}\tilde{\nu}_\mu, \quad \hat{r}_0 + \hat{v}_r t_* = \kappa_{r\mu}\tau_\mu, \tag{30}$$

where the coefficients

$$\begin{aligned} \kappa_{v\mu} &= \overline{\left[h_{m(m+\mu)}(\omega_0)\right]}^{-1}, \\ \kappa_{r\mu} &= \overline{\left[dh_{m(m+\mu)}(\omega_0)/d\omega\right]}^{-1} \end{aligned} \tag{31}$$

determine the spatial and frequency scales of the waveguide transfer function variability [37].

The estimates of the source parameters, in contrast to their true values, are denoted by the dot on top. Bars above an expressions denote the averaging over mode numbers. The value t_* is a point in the observation interval Δt ($0 < t_* < \Delta t$). For the first focal spot, $\mu = 1$, the relation Eq. (31) can be simplified as follows

$$\begin{aligned} \kappa_{v1} &= (M-1)\left[h_{1M}(\omega_0)\right]^{-1} \\ \kappa_{r1} &= (M-1)\left[dh_{1M}(\omega_0)/d\omega\right]^{-1} \end{aligned} \tag{32}$$

Using expressions Eq. (30), Eq. (31), the waveguide invariant [2]

$$\beta = -\frac{h_{mn}(\omega_0)}{\omega_0\left[dh_{mn}(\omega_0)/d\omega\right]} \tag{33}$$

can be written in the form

$$\beta = -\frac{\tilde{v}_\mu \hat{r}_0}{\omega_0 \tau_\mu \hat{v}_r}. \tag{34}$$

An interferogram is observable if the spectrum width $\Delta\omega$ is several times greater than the smallest interference frequency period [37]

$$\Lambda = \frac{2\pi}{r\left|\left(dh_1(\omega_0)/d\omega\right) - \left(dh_M(\omega_0)/d\omega\right)\right|}. \tag{35}$$

As a criterion for the interferogram observability, we take the following inequality

$$\Delta\omega \geq 2\Lambda. \tag{36}$$

It is equivalent to observing one or more fringes. The minimum source distance from the receiver, corresponding to the condition, is estimated as

$$r_{\min} = \frac{4\pi}{\Delta\omega\left|\left(dh_1(\omega_0)/d\omega\right) - \left(dh_M(\omega_0)/d\omega\right)\right|}. \tag{37}$$

With increasing bandwidth and decreasing center frequency of the spectrum, the minimum distance decreases when interferometric methods are used.

Two adjacent focal spots can be distinguished from each other according to the Rayleigh criterion if their maximum positions diverge by more than half the width of the spot. The following inequality applies

$$\Delta\omega r_0 \left| \frac{d\overline{h_{m(m+\mu)}(\omega_0)}}{d\omega} - \frac{d\overline{h_{m(m+\mu+1)}(\omega_0)}}{d\omega} \right| \geq 2\pi, \tag{38}$$

$$\Delta t |w| \left| \overline{h_{m(m+\mu)}(\omega_0)} - \overline{h_{m(m+\mu+1)}(\omega_0)} \right| \geq 2\pi. \tag{39}$$

Increasing the distance, bandwidth, radial velocity and observation time leads to an increase in the resolution of interferometric processing. Failure to satisfy the conditions Eq. (38), Eq. (39) leads to superposition of adjacent focal points. The maxima spread out and the errors in radial velocity and source spacing increase. We adhere to this interpretation of the focal spot configuration even in the case of the small number of modes.

The localization method is robust to small perturbations of the marine environment parameters. This is because the solution of the inverse problem is determined by the difference between the propagation constants and their frequency derivatives for the different numbers of perturbation modes. This property underlies the concept of waveguide invariant [2]. The stability of the method to changes in oceanic bottom parameters is experimentally illustrated in [13].

In practice, the proposed processing method is relatively simple to implement. During the observation time Δt in the radiation band $\Delta\omega J$ independent realizations of duration t_s and a time interval between them δt_s are accumulated

$$J = \frac{\Delta t}{t_s + \delta t_s} \tag{40}$$

Implementations are uncorrelated if $\delta t_s > 2\pi/\Delta\omega$. An interferogram $I(\omega, t)$ is formed and a two-dimensional Fourier transform is applied to it in the time-frequency variables. At the output of the integral transform, the spectral density is localized. The linear size of this region is small compared to the size of the interferogram. The solution of the inverse problem based on the estimation of the coordinates of the maxima of the focal spots is performed with a time delay of Δt. The transfer function of an oceanic waveguide can be considered as a two-dimensional linear time-frequency (spatial) filter. In this sense, the proposed method can be considered as a two-dimensional optimal filtering on receiving a given signal.

6. Numerical Simulation Results

The waveguide model is similar in characteristics to the experimental channel (see Fig. 9). The waveguide depth is $H = 53$ m. The water layer sound velocity profile is constant $c(z) = 1470$ m/s. The liquid absorbing bottom parameters: refractive index is $0.86(1 + \mathrm{i}0.01)$, density is $\rho_b = 1.8$ g/cm^3. The sound source at a depth of $z_s = 15$ m moves along the trajectory shown in Fig. 1. The source speed is $v = 1.7$ m/s. The frequency band is $\Delta f = 40$ Hz (180–220 Hz). The receiver is located in point Q at a depth of $z_q = 53$ m.

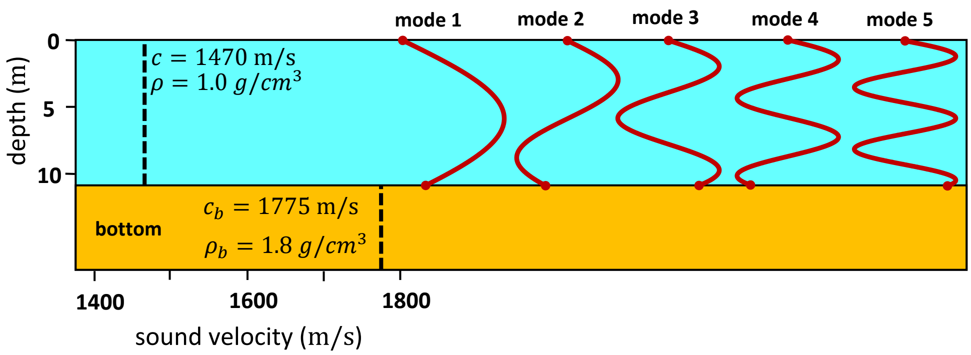

Figure 9. The model waveguide parameters for the numerical simulation.

Our numerical analysis assumes that the sound field is formed by a broadband source with spectrum $S(\omega) = \mathrm{const}$ at the point $S\,(\vec{r}_s(t), z_s(t))$. The velocity of motion of the source is $\vec{v}$. Using the acoustic vertical modes shown in Fig. 9, Eq. (1) is obtained for the pressure field. The $\phi_m(z,\omega)$ are the eigenfunctions (modes) and $h_m(\omega)$ and $\gamma_m(\omega)/2$ are the real and imaginary parts of the eigenvalues (horizontal wave numbers) $\xi_m(\omega) = h_m(\omega) + \mathrm{i}\gamma_m(\omega)/2$ obtained by solving the Sturm-Liouville problem under the usual boundary conditions [30].

$$\begin{gathered} \text{in water layer} \quad (0 \le z \le H): \\ \frac{d^2\phi_m(z,\omega)}{dz^2} + \{k^2 n^2(z) - \xi_m^2(\omega)\}\phi_m(z,\omega) = 0; \\ \text{in bottom} \quad (z > H): \\ \frac{d^2\phi_m(z,\omega)}{dz^2} + \{k^2 n_b^2(z) - \xi_m^2(\omega)\}\phi_m(z,\omega) = 0; \end{gathered} \tag{41}$$

with boundary conditions:

$$\phi_m(z,\omega)\big|_{z=0} = 0,$$
$$\phi_m(z,\omega)\big|_{z=H-0} = \phi_m(z,\omega)\big|_{z=H+0},$$
$$\frac{1}{\rho}\frac{d\phi_m}{dz}\Big|_{z=H-0} = \frac{1}{\rho_b}\frac{d\phi_m}{dz}\Big|_{z=H+0}$$

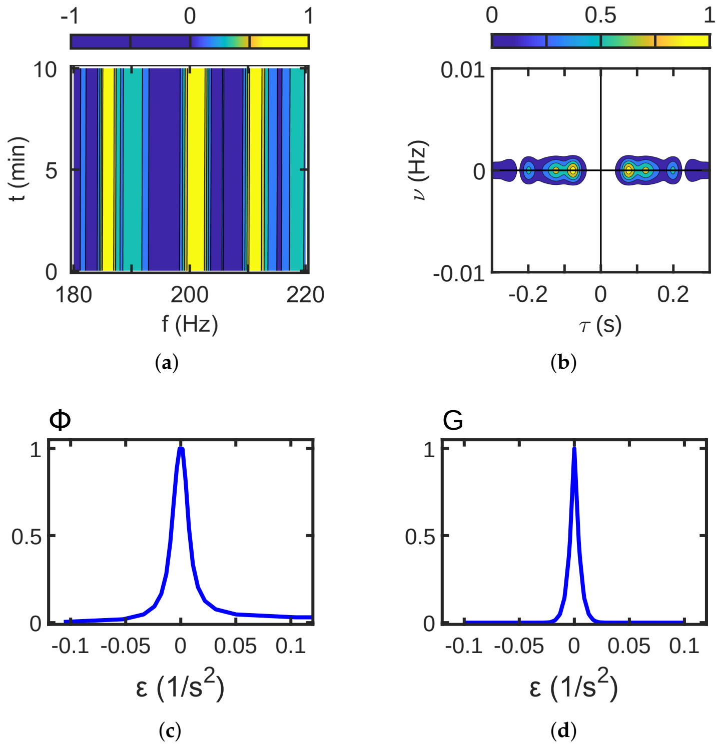

Figure 10. The results of the numerical simulation for case I. The source motion between A and B. Normalized interferogram $I(f,r)$ - (a), normalized hologram $F(\tau,\nu)$ - (b), normalized angular interferogram distribution $\Phi(\varepsilon)$ - (c), normalized angular hologram distribution $G(\varepsilon)$ - (d).

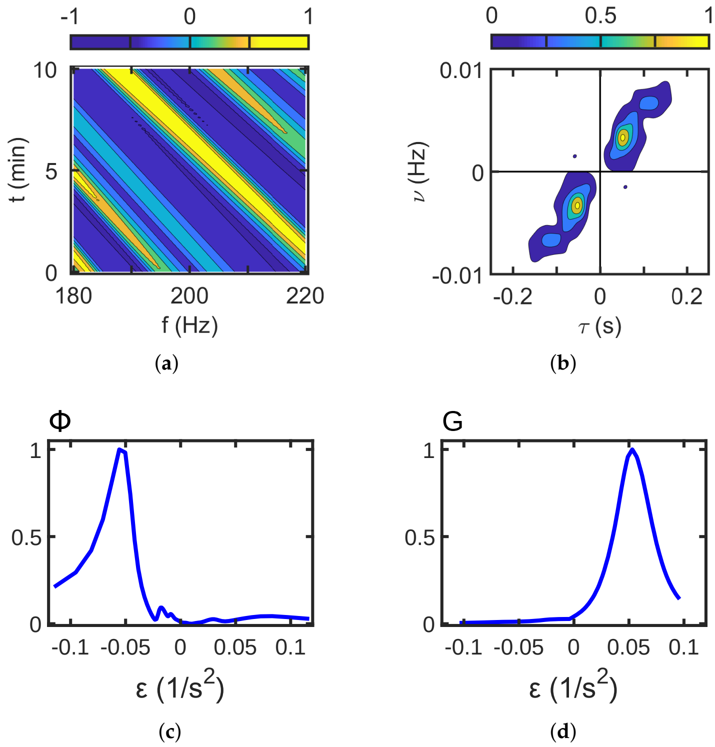

Figure 11. The results of the numerical simulation for case II. The source motion between B and C. Normalized interferogram $I(f, r)$ - (a), normalized hologram $F(\tau, \nu)$ - (b), normalized angular interferogram distribution $\Phi(\varepsilon)$ - (c), normalized angular hologram distribution $G(\varepsilon)$ - (d).

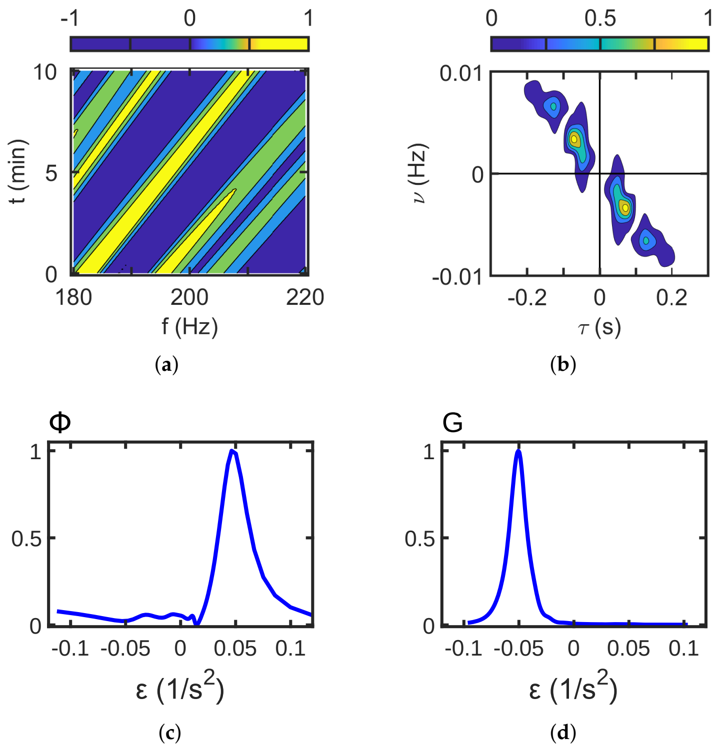

Figure 12. The results of the numerical simulation for case III. The source motion between C and D. Normalized interferogram $I(f, r)$ - (a), normalized hologram $F(\tau, \nu)$ - (b), normalized angular interferogram distribution $\Phi(\varepsilon)$ - (c), normalized angular hologram distribution $G(\varepsilon)$ - (d).

Three cases of source motion (Fig. 1) are considered using the simulated data.
I) Source moves along an arc from A to B around receiver Q :

$$r(t) = |\vec{r}_q - \vec{r}_s(t)| = r_0, \ \ r_0 = 11\,\mathrm{km}, \ \ v = 1.7\,\mathrm{m/s},$$
$$0 \leqslant t \leqslant 10\,\mathrm{min}, \ \ 180 \leqslant f \leqslant 220\,\mathrm{Hz}.$$

II) Source approaches to receiver Q along straight-line path from B to C:

$$r(t) = |\vec{r}_q - \vec{r}_s(t)| = r_0 - vt, \ \ r_0 = 7\,\mathrm{km}, \ \ v = 1.7\,\mathrm{m/s},$$
$$0 \leqslant t \leqslant 10\,\mathrm{min}, \ \ 180 \leqslant f \leqslant 220\,\mathrm{Hz}, \ \ 6\,\mathrm{km} \leqslant r(t) \leqslant 7\,\mathrm{km}.$$

III) Source moves away from receiver Q along a straight-line path from C to D:

$$r(t) = |\vec{r}_q - \vec{r}_s(t)| = r_0 + vt, r_0 = 6\,\mathrm{km}, \ \ v = 1.7\,\mathrm{m/s},$$
$$0 \leqslant t \leqslant 10\,\mathrm{min}, \ \ 180 \leqslant f \leqslant 220\,\mathrm{Hz}, \ \ 6\,\mathrm{km} \leqslant r(t) \leqslant 7\,\mathrm{km}.$$

The results of the processing of the simulated data are shown in Fig. 10, Fig. 11, Fig. 12. The different cases of the source motion are considered. The dynamics of normalized interferogram $I(f,r)$ (Eq. (5)) is shown in Fig. 10 (a), Fig. 11 (a), Fig. 12 (a). The dynamics of normalized hologram $F(\tau,\nu)$ (Eq. (21)) is shown in Fig. 10 (b), Fig. 11 (b), Fig. 12 (b). The dynamics of normalized angular interferogram distribution $G(\varepsilon)$ (Eq. (19)) is shown in Fig. 10 (c) Fig. 11 (c), Fig. 12 (c). The dynamics of normalized angular hologram distribution $\Phi(\varepsilon)$ (Eq. (29)) is shown in Fig. 10 (d) Fig. 11 (d), Fig. 12 (d).

The interferogram in Fig. 10 (a), hologram in Fig. 10 (b), angular interferogram and hologram distributions in Fig. 10 (c,d) correspond to case I: source moves along the arc of radius $r_0 = 11$ km from point A to point B. Interference fringes are localized along vertical lines. On the hologram, the focal spots are located on the time τ-axis. The main maximum coordinate is $\tau_1 = 0.077$ s. The maximum of angular interferogram and hologram distributions (Fig. 10 (c,d)) is $\varepsilon_I = \varepsilon_F = 0\,\mathrm{s}^{-2}$. In result, we have the following estimations of the radial velocity and the distance of source (Eq. (30)): $\dot{v}_r = 0$ m/s and $\dot{r} = 11.3$ km.

The normalized interferogram $I(f,t)$, hologram $F(\tau,\nu)$ and angular interferogram and hologram distributions $\Phi(\varepsilon)$ $G(\varepsilon)$ in Fig. 11(a,b,c,d) for case II: source approaches to receiver Q along straight-line path from B to C. The slope ratio of the interference fringes is equal $\delta f/\delta t = -0.05\ \mathrm{s}^{-2}$(see Fig. 11(a)). The maximum of angular interferogram distribution $\Phi(\varepsilon)$ is $\varepsilon_I = -0.05\ \mathrm{s}^{-2}$ (Fig. 11(c)). The maximum of angular hologram distribution $G(\varepsilon)$ is $\varepsilon_F = 0.05\ \mathrm{s}^{-2}$ (Fig. 11(d)). The hologram main focal spot coordinates are $\tau_1 = 0.053$ s and $\nu_1 = 0.0032$ Hz (Fig. 11(b)). This gives the following estimates for the radial velocity and the distance of the source (Eq. (30)): $\dot{v}_r = -1.9$ m/s and $\dot{r} = 7.3$ km.

The normalized $I(f,t)$, hologram $F(\tau,\nu)$ and angular interferogram and hologram distributions $\Phi(\varepsilon)$, $G(\varepsilon)$ in Fig. 12(a,b,c,d) for case III: source moves away from receiver Q along a straight-line path from C to D. The slope ratio of the interference fringes is equal $\delta f/\delta t = 0.05\ \mathrm{s}^{-2}$ (see Fig. 12(a)).

The maximum of angular interferogram distribution $\Phi(\varepsilon)$ is $\varepsilon_I = 0.05\ \mathrm{s}^{-2}$ (Fig. 12(c)). The maximum of angular hologram distribution $G(\varepsilon)$ is $\varepsilon_F = -0.05\ \mathrm{s}^{-2}$ (Fig. 12(d)). The hologram main focal spot coordinates are $\tau_1 = 0.05$ s and $\nu_1 = -0.0033$ Hz (Fig. 12(b)). This gives the following estimates for the radial velocity and the distance of the source (Eq. (30)): $\dot{v}_r = 1.9$ m/s and $\dot{r} = 7.2$ km.

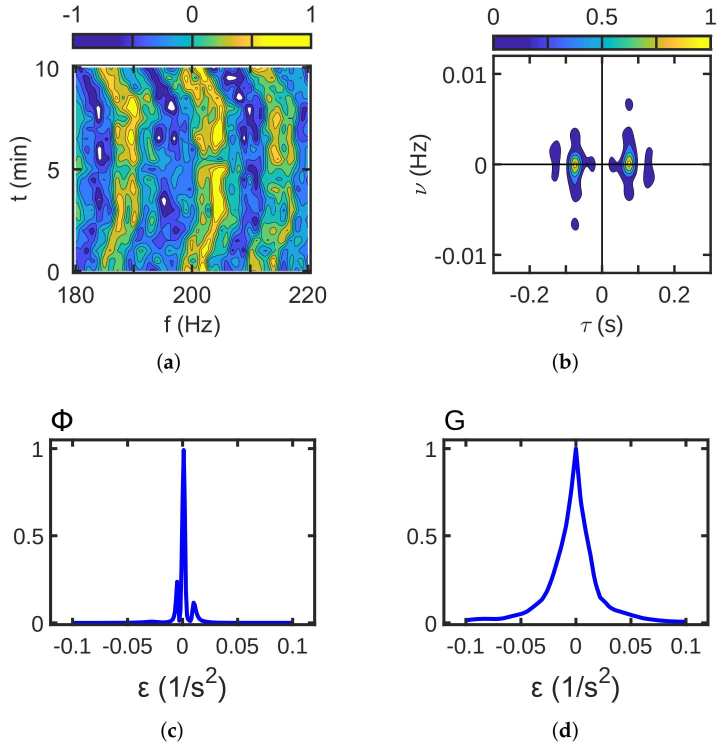

Figure 13. The experimental results for case I. The source motion between A and B. Normalized interferogram $I(f,r)$ - (a), normalized hologram $F(\tau,\nu)$ - (b), normalized angular interferogram distribution $\Phi(\varepsilon)$ - (c), normalized angular hologram distribution $G(\varepsilon)$ - (d).

7. Experimental Results

The results of the experimental data processing are shown in Figs. 13–15. The different cases of the source motion are considered. The dynamics of normalized interferogram $I(f,r)$ (Eq. (5)) is shown in Fig. 13 (a), Fig. 14 (a), Fig. 15 (a).

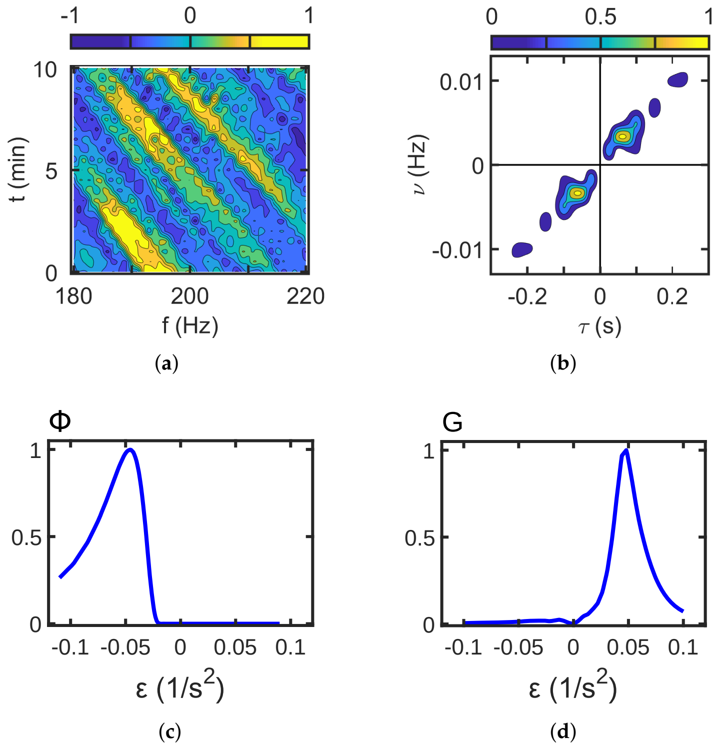

Figure 14. The experimental results for case II. The source motion between B and C. Normalized interferogram $I(f,r)$ - (a), normalized hologram $F(\tau,\nu)$ - (b), normalized angular interferogram distribution $\Phi(\varepsilon)$ - (c), normalized angular hologram distribution $G(\varepsilon)$ - (d).

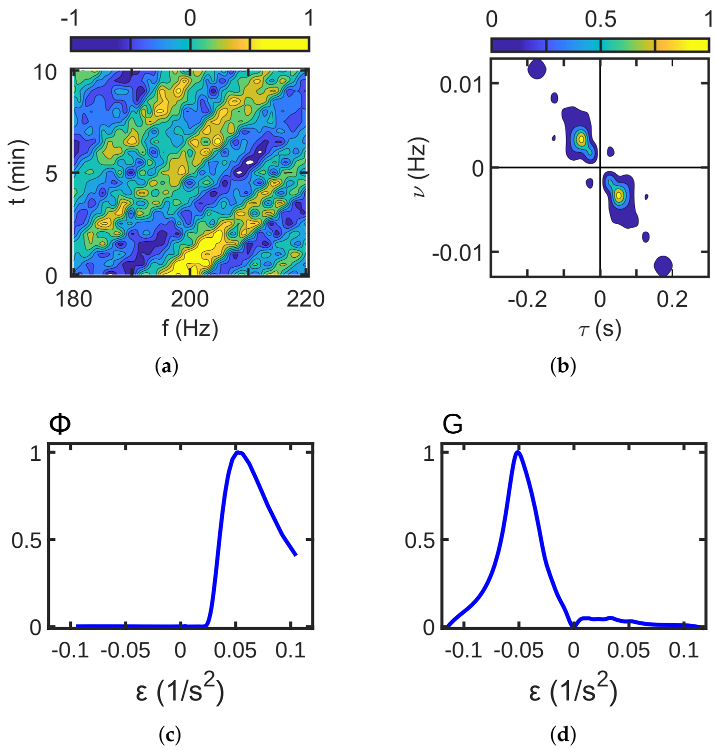

Figure 15. The experimental results for case III. The source motion between C and D. Normalized interferogram $I(f,r)$ - (a), normalized hologram $F(\tau,\nu)$ - (b), normalized angular interferogram distribution $\Phi(\varepsilon)$ - (c), normalized angular hologram distribution $G(\varepsilon)$ - (d).

The dynamics of normalized hologram $F(\tau, \nu)$ (Eq. (21)) is shown in Fig. 13 (b), Fig. 14 (b), Fig. 15 (b). The dynamics of normalized angular interferogram distribution $G(\varepsilon)$ (Eq. (19)) is shown in Fig. 13 (c) Fig. 14 (c), Fig. 15 (c). The dynamics of normalized angular hologram distribution $\Phi(\varepsilon)$ (Eq. (29)) is shown in Fig. 13 (d) Fig. 14 (d), Fig. 15 (d).

The interferogram in Fig. 13 (a) and the hologram in Fig. 13 (b) correspond to the motion of the source along the arc of radius $r_0 \approx 11$ km between point A and point B. It can be seen that the interference bands are different from the vertical lines. This implies that the path of the source deviates from a circular arc. At the same time, the position of the main hologram peaks on the time axis (Fig. 13 (b)) indicates that the radial velocity of the source is zero. The presence of two peaks in the hologram (Fig. 13 (b)) indicates that the field is formed by three modes. Note that the interferogram and hologram are identical for a stationary source and for a source moving along an arc. The value of the arc radius r_0 can be estimated from the formula Eq. (30) assuming that the radial velocity $v_r = 0$. As shown in Fig. 13 (b), $\tau_1 = 0.074$ s. Under the experimental conditions at the reference frequency $f_0 = 100$ Hz, the group velocities u_1 and u_3 are 1467.0 m/s and 1438.4 m/s, respectively. This results in $r_0 = 10.9$ km.

The sound field interferogram and hologram for a source moving from point B to point C (after VSR Q) are shown in Figs. 14 (a) and (c). The sound field interferogram and hologram for a source moving from point C to point D (away from VSR Q) are in Fig. 15 (a) and (c). The interference patterns (Figs. 14 (a), Figs. 15 (a)) consist of straight-line localized bands. This shows that the direction of motion and the radial velocity of the source are constant. The slopes of the bands have opposite signs for different source directions. Compared to the case of a source moving along the arc from A to B, the holograms have more main peaks. This indicates the increasing number of sound field modes. For a source moving to VSR Q the maximum of angular interferogram distribution $\Phi(\varepsilon)$ is $\varepsilon_I = -0.05$ s^{-2} (Fig. 14(c)). The maximum of angular hologram distribution $G(\varepsilon)$ is $\varepsilon_F = 0.05$ s^{-2} (Fig. 14(d)). The coordinates of the main peaks are $\tau_1 = 0.056$ s and $\nu_1 = 0.0031$ Hz (Fig. 14 (b)). For a source motion from VSR Q the maximum of angular interferogram distribution $\Phi(\varepsilon)$ is $\varepsilon_I = 0.05$ s^{-2} (Fig. 15(c)). The maximum of angular hologram distribution $G(\varepsilon)$ is $\varepsilon_F = -0.05$ s^{-2} (Fig. 15(d)). The coordinates of the main peaks are $\tau_1 = 0.056$ s, $\nu_1 = -0.0031$ Hz (Fig. 15 (b)). This yields the following estimates for the radial velocity and distance to the source: $v_r = -1.9$ m/s and $r = 7.8$ km for the case of source motion toward VSR Q and $v_r = 1.9$ m/s and $r = 7.7$ km for the case of source motion away from VSR Q.

One can see that results presented in the Section 7 for solving the inverse problem of source localization in the numerical simulation agree well with the numerical model parameters and are consistent with the results of the acoustic experiment presented in Section 6.

8. Conclusions

The results of the analysis of the interference pattern of the sound field of a broadband source in shallow water are presented in this paper. The experimental recordings are processed to obtain interferograms for different paths of the source motion. The Fourier hologram is used to analyze the experimental interferograms. It is shown that the hologram shows a coherent accumulation of the sound intensity of the interferogram in a narrow area as focal peaks coherently accumulate along the line passing through the origin. Further, we have shown that the position of the focal spots in the experimental hologram depends on the radial velocity of the source, the direction of motion, and the distance to the receiver. The position of the main hologram peaks is on the time axis as the source moves along the arc. It means that the radial velocity of the source is zero. The hologram peaks are located in quadrants I and III when the source is moving towards the receiver. In case of the source movement away from the receiver, the hologram peaks are located in quadrants II and IV. The estimates of the source parameters are presented for different directions of the source motion in the experiment. The good agreement between the experimental and estimated values shows the efficiency of this approach for solving source localization problems. Thus, it is possible to use interferograms and holograms as a potential basis for the application of holographic interferometry in passive source location. This approach allows the complex problem of detecting a source and estimating its speed, distance, and depth to use only a single receiver.

Author Contributions: Supervision and project administration, M.E.; conceptualization and methodology, V.K. and S.P.; software, K.I. and P.R.; validation, M.E. and V.K.; formal analysis, M.E. and S.P.; writing – original draft preparation, M.E and S.P.; writing – review and editing, M.E. and S.P.; All authors have read and agreed to the published version of the manuscript.

Funding: This research was supported by the Russian Foundation for Basic Research (project no. 19-29-06075). Kaznacheev I.V. was supported by the grant of the President of the Russian Federation, (project no. MK-4846.2022.4).

References

1. D. Weston and K. Stevens, "Interference of wide-band sound in shallow water," Journal of Sound and Vibration **21**(1), 57–64 (1972).
2. S. Chuprov, "Interference structure of a sound field in a layered ocean," Ocean Acoustics, Current State 71–91 (1982).
3. G. Grachev and J. Wood, "Theory of acoustic field invariants in layered waveguides," Acoustical Physics **39**(1), 33–35 (1993).
4. Orlov, E. F., and Sharonov, G. A. (**1998**). "Interference of sound waves in the ocean," (Dal'nauka).
5. W. A. Kuperman and G. L. D'Spain, "Ocean acoustic interference phenomena and signal processing," Ocean Acoustic Interference Phenomena and Signal Processing **621** (2002).
6. G. Kuznetsov, V. Kuz'kin, S. Pereselkov, and I. Kaznacheev, "Noise source localization in shallow water," Physics of Wave Phenomena **25**(2), 156–163 (2017).
7. A. M. Thode, "Source ranging with minimal environmental information using a virtual receiver and waveguide invariant theory," The Journal of the Acoustical Society of America **108**(4), 1582–1594 (2000).
8. K. L. Cockrell and H. Schmidt, "Robust passive range estimation using the waveguide invariant," The Journal of the Acoustical Society of America **127**(5), 2780–2789 (2010).
9. I. Kaznacheev, G. Kuznetsov, V. Kuz'kin, and S. Pereselkov, "An interferometric method for detecting a moving sound source with a vector-scalar receiver.," Acoustical Physics **64**(1), 37–48 (2018).
10. S. Pereselkov, V. Kuz'kin, "Interferometric processing of hydroacoustic signals for the purpose of source localization," The Journal of the Acoustical Society of America **151**(2), 666–676 (2022).
11. R. Emmetiere, J. Bonnel, X. Cristol, M. Géhant, and T. Chonavel, "Passive source depth discrimination in deep-water," IEEE Journal of Selected Topics in Signal Processing **13**(1), 185–197 (2019).
12. G. Kuznetsov, V. Kuz'kin, and S. Pereselkov, "Spectrogram and localization of a sound source in shallow water," Acoustical Physics **63**(4), 449–461 (2017).
13. G. Kuznetsov, V. Kuz'kin, S. Pereselkov, I. Kaznacheev, and V. Grigor'ev, "Interferometric method for estimating the velocity of a noise sound source and the distance to it in shallow water using a vector-scalar receiver," Physics of Wave Phenomena **25**(4), 299–306 (2017).
14. G. Kuznetsov, V. Kuz'kin, S. Pereselkov, and D. Y. Prosovetskiy, "Wave method for estimating the sound source depth in an oceanic waveguide," Physics of Wave Phenomena **24**(4), 310–316 (2016).
15. R. Emmetière, J. Bonnel, M. Géhant, X. Cristol, and T. Chonavel, "Understanding deep-water striation patterns and predicting the waveguide invariant as a distribution depending on range and depth," The Journal of the Acoustical Society of America **143**(6), 3444–3454 (2018).
16. A. Turgut, M. Orr, and D. Rouseff, "Broadband Source Localization Using Horizontal-Beam," The Journal of the Acoustical Society of America **127**(1), 73–83 (2010).
17. Quijanoa, J. E., Zurk, L. M., and Rouseff, D. (**2008**). "Demonstration of the invariance principle for active sonar The Journal of the Acoustical Society of America **123**(3)," 1329–1337.
18. L. M. Zurk and D. Rouseff, "Striation-based beamforming for active sonar with a horizontal line array," The Journal of the Acoustical Society of America **132**(4), EL264–EL270 (2012).
19. K. D. Heaney, "Rapid geoacoustic characterization using a surface ship of opportunity," IEEE Journal of Oceanic Engineering **29**(1), 88–99 (2004).
20. J. Bonnel, G. Le Touzé, B. Nicolas, and J. I. Mars, "Physics-based time-frequency representations for underwater acoustics: Power class utilization with waveguide-invariant approximation," IEEE Signal Processing Magazine **30**(6), 120–129 (2013).
21. Y. Le Gall and J. Bonnel, "Separation of moving ship striation patterns using physics-based filtering," in *Proceedings of Meetings on Acoustics ICA2013*, Acoustical Society of America (2013), Vol. 19, p. 070073.
22. M. Badiey, V. Kuz'kin, and S. Pereselkov, "Interferometry of hydrodynamics of oceanic shelf caused by intensive internal waves," Fundamental and Applied Hydrophysics **13**(1), 45–55 (2020).

23. D. Rouseff, "Effect of shallow water internal waves on ocean acoustic striation patterns," Waves in Random Media **11**(4), 377 (2001).
24. D. Rouseff and R. C. Spindel, "Modeling the waveguide invariant as a distribution," in *AIP Conference Proceedings*, American Institute of Physics (2002), Vol. 621, pp. 137–150.
25. A. B. Baggeroer, "Estimation of the distribution of the interference invariant with seismic streamers," in *AIP Conference Proceedings*, American Institute of Physics (2002), Vol. 621, pp. 151–170.
26. T. Yang, "Beam intensity striations and applications," The Journal of the Acoustical Society of America **113**(3), 1342–1352 (2003).
27. C. H. Harrison, "The relation between the waveguide invariant, multipath impulse response, and ray cycles," The Journal of the Acoustical Society of America **129**(5), 2863–2877 (2011).
28. A. B. Baggeroer, W. A. Kuperman, and P. N. Mikhalevsky, "An overview of matched field methods in ocean acoustics," IEEE Journal of Oceanic Engineering **18**(4), 401–424 (1993).
29. J. Ianniello, "Recent developments in sonar signal processing," IEEE Signal Processing Magazine **15**(4), 27–40 (1998).
30. F. B. Jensen, W. A. Kuperman, M. B. Porter, H. Schmidt, and A. Tolstoy, *Computational Ocean Acoustics*, Vol. 2011 (Springer, 2011).
31. C. W. Bogart and T. Yang, "Comparative performance of matched-mode and matched-field localization in a range-dependent environment," The Journal of the Acoustical Society of America **92**(4), 2051–2068 (1992).
32. H. P. Bucker, "Use of calculated sound fields and matched-field detection to locate sound sources in shallow water," The Journal of the Acoustical Society of America **59**(2), 368–373 (1976).
33. J. Capon, "High-resolution frequency-wavenumber spectrum analysis," Proceedings of the IEEE **57**(8), 1408–1418 (1969).
34. H. Chandler, C. Feuillade, and G. Smith, "Sector-focused processing for stabilized resolution of multiple acoustic sources," The Journal of the Acoustical Society of America **97**(4), 2159–2172 (1995).
35. R. Schmidt, "Multiple emitter location and signal parameter estimation," IEEE Transactions on Antennas and Propagation **34**(3), 276–280 (1986).
36. M. Bengtsson and B. Ottersten, "A generalization of weighted subspace fitting to full-rank models," IEEE transactions on signal processing **49**(5), 1002–1012 (2001).
37. L. M. Brekhovskikh and Y. P. Lysanov, *Fundamentals of Ocean Acoustics* (Springer, 2013).